The GlueX Start Counter Detector

E. Pooser[a,b,*], F. Barbosa[a], W. Boeglin[b], C. Hutton[a], M. Ito[a], M. Kamel[b], P. Khetarpal[b], A. LLodra[b], N. Sandoval[a], S. Taylor[a], C. Yero[b], T. Whitlatch[a], S. Worthington[a], B. Zihlmann[a]

[a] *Thomas Jefferson National Accelerator Facility, Newport News, VA 23606, USA*
[b] *Florida International University, Miami, FL, 33199, USA*

Abstract

The design, fabrication, calibration, and performance of the GlueX Start Counter detector is described. The Start Counter was designed to operate at photon intensities of up to $10^8\gamma$/s in the coherent peak and provides a timing resolution of ≈ 280 ps thus providing successful identification of the photon beam buckets to more than 99% accuracy. Furthermore, the Start Counter provides excellent solid angle coverage, $\sim 90\%$ of 4π hermeticity, a high degree of segmentation for background rejection, and is utilized in the level 1 trigger for the experiment. It consists of a cylindrical array of 30 thin scintillators with pointed ends that bend towards the beam at the downstream end. Magnetic field insensitive silicon photomultiplier detectors were selected as the readout system.

Keywords: Attenuation, F1 TDC, Flash 250 MHz ADC, GlueX, Multi-Pixel Photon Counter, Particle Identification, Plastic Scintillator, Polishing Scintillators, Propagation Time, Silicon Photomultiplier, Time of Flight, Time-walk, Trigger

1. Introduction

The GlueX experiment, staged in Hall D at the Thomas Jefferson National Accelerator Facility (TJNAF), primarily aims to study the spectrum of photo-produced mesons with unprecedented statistics. The coherent bremsstrahlung technique is implemented to produce a linearly polarized photon beam incident on a liquid H_2 target. A Start Counter detector was fabricated to properly identify the photon beam buckets and to provide accurate timing information.

2. Design

In this section we discuss the details of the GlueX Start Counter design. The general engineering specifics pertaining to the scintillators, support structure, detector readout system and electronics are discussed.

2.1. Overview

The Start Counter detector (ST), seen in Fig. 1, surrounds a 30 cm long super cooled liquid H_2 target while providing $\sim 90\%$ of 4π solid angle coverage relative to the target center. The primary

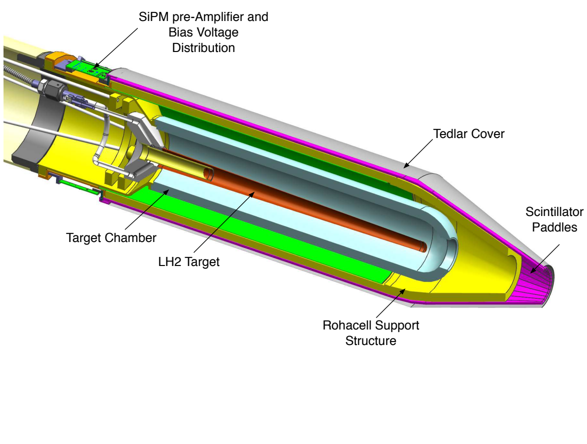

Figure 1: The GlueX Start Counter mounted to the liquid H_2 target. The beam direction is oriented from left to right down the central axis of the ST.

*Corresponding Author
Email address: pooser@jlab.org (E. Pooser)

purpose of the ST is, in coincidence with the tagger, to properly identify the photon beam bucket associated with detected particles produced by linearly polarized photons incident on the target. It is designed to operate at tagged photon intensities of up to $10^8\ \gamma$/s in the coherent peak. Moreover, the ST has a high degree of segmentation for background rejection, is utilized in particle identification, and is a primary component of the level 1 trigger of the GlueX experiment during high luminosity running[1].

The ST consists of an array of 30 scintillators with pointed ends that bend towards the beam at the downstream end. EJ-200 scintillator material

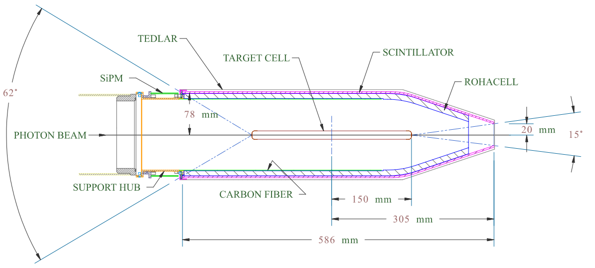

Figure 2: 2-D cross section of the Start Counter.

from Eljen Technology[2], which has a decay time of 2.1 ns and a long attenuation length[3], was selected for this application. The amount of support structure material was kept to an absolute minimum in the active region of the detector and is made up of low density Rohacell[4]. Silicon Photomultiplier (SiPM) detectors were selected as the readout system. The detectors are not affected by the high magnetic field produced by the superconducting solenoid magnet. Moreover, the SiPMs were placed as close as possible to the upstream end of each scintillator element, thereby minimizing the loss of scintillation light[1].

2.2. Scintillator Paddles

Each individual paddle of the Start Counter was machined from a long, thin, EJ-200 scintillator bar that was diamond milled to be 600 mm in length, 3 mm thick, and 20 ± 2 mm wide, by Eljen Technology. Each scintillator was bent around a highly polished aluminum drum by applying localized infrared heating to the bend region. The bent scintillator bars were then sent to McNeal Enterprises Inc.[5], a plastic fabrication company, where they were machined to the desired geometry illustrated in Fig. 3.

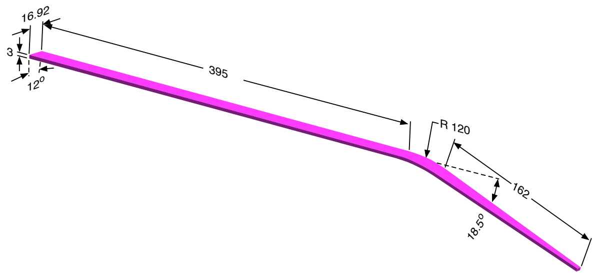

Figure 3: Start Counter single paddle geometry. Unlabeled dimensions shown are in mm.

The paddles consist of three sections and are described from the upstream to the downstream end of the target. The straight section is 39.5 cm in length while being oriented parallel to both the target cell and beamline. The bend region is a 18.5° arc of radius 120 cm and is downstream of the straight section. The tapered nose region is downstream of the target chamber and bends towards the beam line such that the tip of the nose is at a radial distance of 2 cm from the beam line.

After the straight scintillator bar was bent to the desired geometry, the two flat surfaces that are oriented orthogonal to the wide, top and bottom, surfaces were cut at a 6° angle. During this process, the width of the top and bottom surfaces of the straight section were machined to be 16.92 mm and 16.29 mm wide respectively. Thus, each of the paddles may be rotated 12° with respect to the paddle that preceded it so that they form a cylindrical shape with a conical end. This geometrical design for the ST increases solid angle coverage while minimizing multiple scattering.

2.3. Support Structure

The ST scintillator paddles are placed atop a low density Rohacell ($\rho = 0.075$ g/cm^3) foam support structure which envelopes the target vacuum chamber illustrated in Fig. 1. The Rohacell, which is 11 mm thick, is rigidly attached to the upstream support chassis and extends down the length of paddles however, not to include the last few centimeters of the conical nose section. Glued to the inner diameter of the Rohacell support structure are three layers of carbon fiber ($\rho = 1.523$ g/cm^3) each of which are 650 μm thick. A cross section of the ST can be seen in Fig. 1 where the carbon fiber is visible. The carbon fiber provides additional support during the assembly process as well as long term rigidity.

The various layers of material that comprise the ST support structure is illustrated in Fig. 4. In

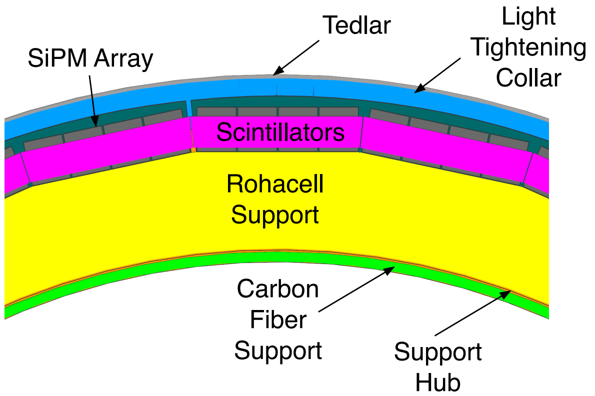

Figure 4: Start Counter materials.

order to ensure that the detector was light-tight, a plastic collar was placed around the top of the SiPMs at the upstream end as seen in Fig. 4. The collar served as a lip to which a cylindrical sheet of black Tedlar was taped too. At the tip of the nose, a cone of Tedlar was then connected to the aforementioned cylindrical section. To make the downstream end of the ST light-tight, another cone of Tedlar was taped to the nose of the inner Rohacell support structure and then attached to the top Tedlar cone layer.

2.4. SiPM Readout Detectors

Each scintillator bar was read out using magnetic field insensitive Hamamatsu S10931-050P multi-pixel photon counters (MPPCs)[6]. An individual 3×3 mm^2 MPPC, also known as a SiPM, in the aforementioned configuration is comprised of 3600 individual, 50×50 μm^2, Avalanche Photo-Diode (APD) pixel counters operating in Geiger mode. The signal output from each SiPM is the total sum of the outputs from all 3600 APD pixels[7]. The scintillation light from an individual scintillator bar is collected by an array of four of these SiPMs. Three groups of four SiPMs comprise what is referred to as the “ST1” of the readout system.

The SiPM detectors are housed in a ceramic case which is surface mounted to a custom fabricated printed circuit board (PCB). The PCB is held in a fixed position while being attached to the lip of the upstream chassis. The individual ST scintillators are coupled *via* an air gap ($< 250 \mu m$) to groups of four SiPMs, seen in Fig. 5, which are set in a circular arrangement.

Figure 5: ST1 of Start Counter read out system. Approximately 72% of the scintillator light is collected at the upstream end. The readout is comprised of 10 ST1 units in total. The units of the ruler shown is in inches.

2.5. Readout Electronics

The SiPMs reading out one individual paddle, are current summed prior to pre-amplification. The output of each preamp is then split; buffered for the analog to digital converter (ADC) output, and amplified for the time to digital converter (TDC) output by a factor five relative to the ADC. The ADC outputs are readout by JLab VME64x 250 MHz Flash ADC modules while the TDC outputs are input into JLab leading edge discriminators, followed by a high resolution 32 channel JLab VME64x F1TDC V2 module. Furthermore, each group of four SiPMs utilizes a thermocouple for temperature monitoring. There are 120 SiPMs in total, for a total of 30 pre-amplifier channels as seen Fig. 6.

There are three components that comprise the ST detector readout system. The first component (ST1), will collect light from three paddles individually and consists of three groups of four SiPMs as can be seen in Fig. 5. In order to fit the geometry of the 30 paddle design, adjacent groups of SiPM’s are rotated by 12° relative to the central group, while the other adjacent group is rotated by −12°. The ST1 implements the current sum and bias distribution for each group of four SiPMs. It also has a thermocouple for temperature monitoring.

The second component (ST2), seen in Fig. 7, houses the signal processing electronics of the

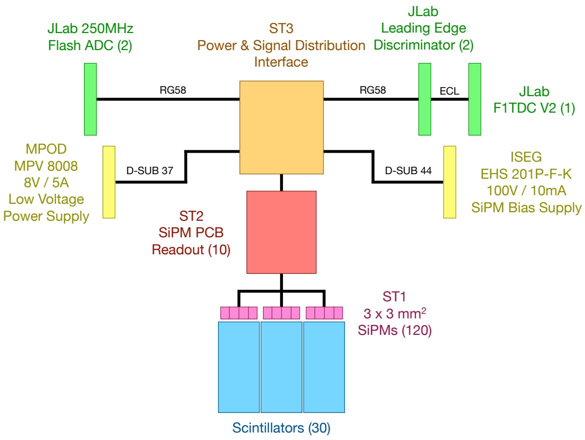

Figure 6: Start Counter readout electronics diagram.

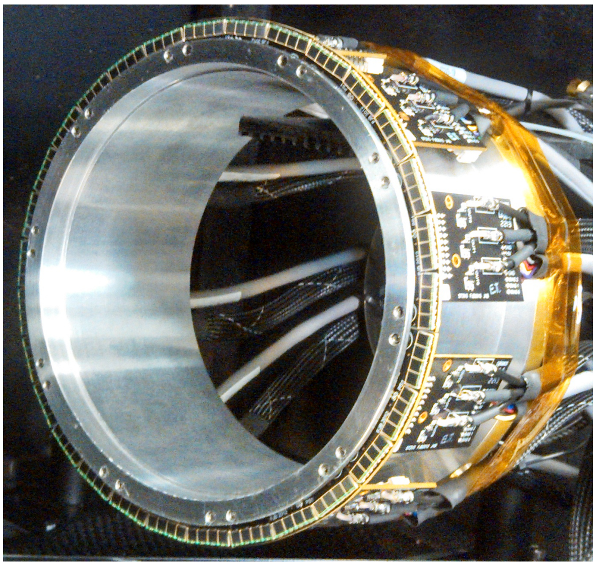

Figure 7: Fully assembled ST readout system. The ST2 unit is connected behind the ST1. The full readout system is comprised of 10 ST2 units.

readout system. It has three channels of pre-amplifiers, three buffers, and three factor-five amplifiers. Furthermore, it has three bias distribution channels with individual temperature compensation *via* thermistors.

The third component of the readout system (ST3) provides the interface to the power and bias supplies. It also routes the ADC and TDC outputs as well as the thermocouple output. The ST3 is installed upstream of the Start Counter and next to the beam pipe.

3. Simulation

In this section, Monte Carlo (MC) simulations of the performance and characteristics of machined scintillators are discussed. These studies were performed using the GEANT4 tool-kit which simulates the passage of particles through matter [8]. Comparisons are made with data observed in experiments conducted on the bench in Sec. 5.2 and with beam data in Sec. 7.

3.1. Simulating a Simplified Model of the ST

As discussed in Sec. 2.2, the ST scintillator paddles have a unique geometry in which the nose section tapers in width as the paddles approach the beam line at the downstream end. This tapering effect results in a unique phenomenon in which the light output of the scintillator paddle begins to increase as the source of scintillation light moves further away from the readout detector. This phenomenon is completely contrary to what one might expect. The conventional sense is that when the source moves further away from the end being readout, the photons have a larger effective path length and thus, have an increased probability in being lost for detection. However, this is antithetical relative to what is observed on the bench and in with beam in Hall-D.

A simple GEANT4 simulation was conducted to investigate the aforementioned phenomenon. The details of the simulation are discussed in Ref. [1]. Only the two trapezoidal regions of a machined scintillator paddle were considered. Namely, the wide straight section and the tapered nose section.

In order to sample the entirety of the two sections, 10,000 optical photons were generated at 16 different locations inside the medium of the scintillator. The photon energies ranged between $0.5 - 3.0$ eV [9] and were generated randomly in 4π along a 3 mm path $(y - axis)$ in the scintillator medium. The path was oriented orthogonal to the wide surface of the scintillator. The number of photons collected by the SiPM at each of the source locations was counted and correlated to the source location. The results can be seen in Fig. 8.

From the data it is clear that the geometry of the nose section results in an improvement of light collection as the source moves further away from the readout detector. In fact, there is a factor $\approx 1/2$

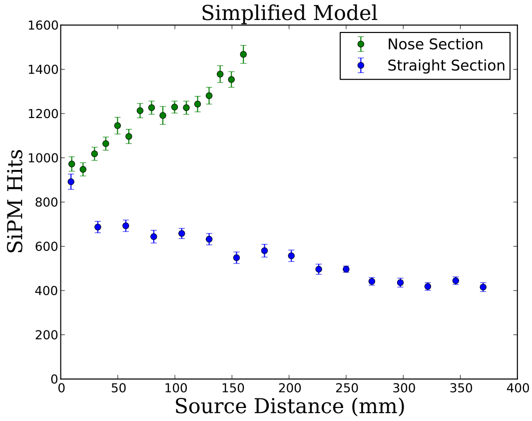

Figure 8: Simulation results for simplified two section scenario. The total number of photons which were collected by the SiPM detector at each of the 16 source locations is plotted against the source distance from the sensitive detector.

light loss observed in the straight section upon comparing the number of hits collected at the closest and furthest locations relative to the readout detector. However, there is factor $\approx 3/2$ light gain observed in the nose region.

These results are primarily due to the tapering trapezoidal geometry in the nose section. This phenomenon is not observed in the quasi-rectangular straight section as it exhibits a more conventional behavior. However, this behavior in the nose region is advantageous under beam conditions in Hall-D since the majority of forward going charged particles will traverse through this region.

3.2. Simulating Machined Scintillator Geometry

Further studies were conducted to simulate more realistically the effects of light collection that results from the ST scintillator geometry and optical surface quality. The ST scintillator geometry was imported into GEANT4 from a Vectorworks CAD drawing utilizing the CADMesh utility [10]. The SiPM was constructed as a $12 \times 12 \times 10\text{mm}^3$ volume with a 100 μm air gap between it and the wide end of the straight section. Furthermore, the volume surrounding the scintillator volume was defined to be air. The EJ-200 scintillator material, SiPM silicon detector, and optical photons were defined in an identical manner discussed in Sec. 3.1.

To simulate the imperfections of the scintillator surfaces due to manufacturing and machining, an optical surface "skin" was defined. The "skin" material was defined to be of the type "dielectric-dielectric" and made use of the POLISH and UNIFIED physics models [11] to define an scintillator surfaces. Both the transmission efficiency and reflection parameters were implemented as free parameters in order to study their various effects on light transmission.

The POLISH model allows for one to simulate a perfectly polished surface while the UNIFIED model allows one to define the finish of the scintillator surface both of which are illustrated in Fig. 9 [11]. The details of the UNIFIED model parameters

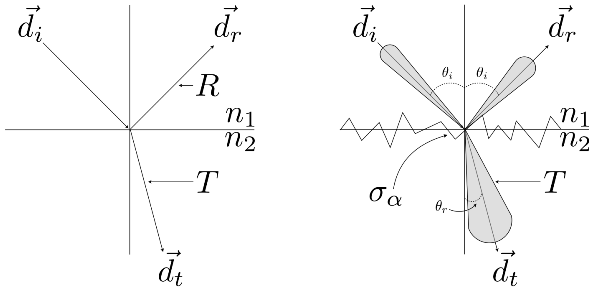

Figure 9: POLISH and UNIFIED models of scintillator surfaces. Left: Polar plot of the radiant intensity of the POLISH model. Right: Polar plot of the radiant intensity in the UNIFIED model [11].

are discussed in detail in Ref. [1] & [11].

As was done in section 3.1, 10,000 optical photons were generated in the scintillator medium every 2.5 cm and the number of hits collected in the SiPM were recorded. For the POLISH model, the transmission efficiency ϵ was varied and the attenuation length α was extracted for various values of ϵ in the straight region. For the UNIFIED model, ϵ was held constant along with the radiant intensity parameters while σ_α, which characterizes the standard deviation of the surfaces micro-facet orientation, was varied. In a similar manner to the POLISH model, α was extracted in order to characterize the attenuation factor of the straight section. The results of these simulations are show in Fig. 10.

It is clear that if the transmission efficiency is increased while assuming a perfectly polished surface, the amount of light collected in the SiPM also increases as illustrated in Fig. 10. Similarly, as the number of micro-facet orientations increase, meaning a more coarsely ground surface, the amount of light collection in the SiPM decreases. Moreover, in the instances where the surface quality of the

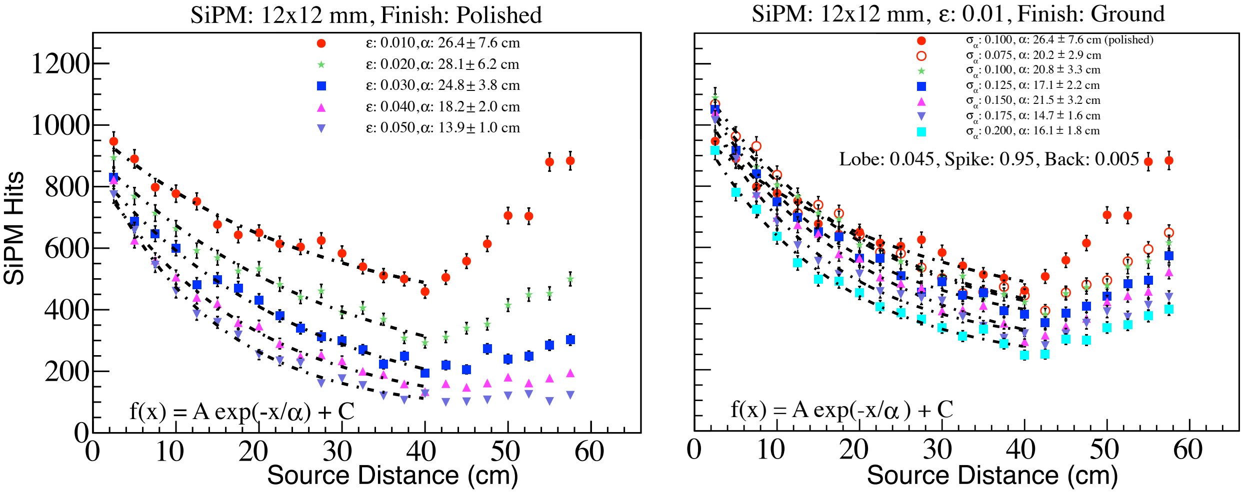

Figure 10: POLISH and UNIFIED model results. The number of hits recorded in the SiPM are plotted on the vertical axis while the source distance (cm) is plotted on the x-axis. Left: POLISH model while varying the transmission efficiency ϵ. Right: UNIFIED model while varying the standard deviation of the surfaces micro-facet orientation σ_α.

machined scintillators are good, the phenomenon of light increase in the nose region as the source moves further from the readout detector is observed.

4. Misalignment Studies

In order to protect both the active area of the SiPMs and the scintillator surface at the upstream end, a small air gap was necessary between these two surfaces. Similarly, during assembly the scintillator paddles were also shimmed radially such that the top edge of the scintillator was level with the top edge of the active area of the SiPM thereby maximizing light collection. In this section we discuss the relative alignment of a machined scintillator paddle and a SiPM readout detector array and its effects on light collection and time resolution.

4.1. Experimental Set-up

A custom fabricated test stand, further discussed in Sec. 5.2, and a polished scintillator machined to the nominal ST geometry, were utilized for the misalignment studies. The readout SiPM sat atop a Newport MT-XYZ (MT) compact dovetail XYZ linear translation stage[12] with three fine adjustment screws consisting of 80 threads per inch. Each knob for the three axes provides a translation of 318 μm per rotation. For each location of the SiPM, the source and trigger PMT were located 24.5 cm downstream from the readout end.

Utilizing an Edmund Optics complementary metal oxide semiconductor (CMOS) camera, both the vertical and horizontal alignment (coupling distance) of the active area of the SiPM and scintillator was measured with 25 μm accuracy. A micrometer,

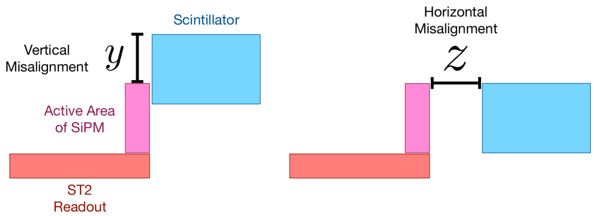

Figure 11: Optics setup for misalignment studies. Left: SiPM & scintillator vertical misalignment. Right: SiPM & scintillator horizontal misalignment

with 25 μm resolution, was utilized in order to cross check the optical measurements and to provide absolute measurements of fixed distances in the experimental set-up. Further details of the experimental set-up are discussed in Ref. [1].

4.2. Vertical Alignment of SiPM & Scintillator

In order to measure the time resolution at various vertical alignment configurations, the scintillator remained fixed while the SiPM scanned across the upstream end of the scintillator (y) as can be seen in the left of Fig. 11. The coupling distance between the active area of the SiPM and scintillator (z) remained at a constant distance of 100 μm and was monitored closely during the vertical alignment scan. We have defined that at $y = 0$ the SiPM and scintillator are aligned vertically.

"Coarse" measurements were then taken at half turn intervals (159 μm) while "precise" measurements were taken in quarter turn intervals (79.5 μm). The results of these measurements can be seen in Fig. 12. The results indicate that there

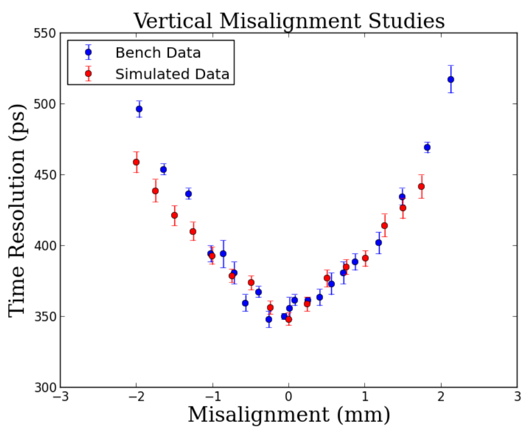

Figure 12: Vertical misalignment results. The minimum time resolution obtained was approximately 350 ps which was expected. Once the SiPM exceeded $y = \pm 3$ mm, no active area of the SiPM was directly coupled to the face of the scintillator.

is no significant variation of time resolution within a ± 300 μm range of the optimal alignment.

Vertical misalignments were also simulated in a manner similar to what was discussed in section 3.2 and the results are seen in Fig. 12. The GEANT4 simulations indicate that the acceptable range of vertical misalignment is approximately ± 250 μm [13] which is consistent with what was measured on the bench.

4.3. Coupling Distance of SiPM & Scintillator

With the vertical alignment between the scintillator and SiPM optimized, the effects of varying the coupling distance were also studied. Using an identical set-up as was described in section 4.2 the coupling distance, and resulting time resolutions, were measured at various locations along z illustrated in Fig. 11. While the coupling distance was varied, the vertical alignment y was kept constant at the optimal location *i.e.* $y = 0$, and was monitored both optically and manually with a micrometer.

The SiPM was moved *via* the MT translation stage along the $z - axis$. We defined $z = 0$ to be the instance when the active area of the SiPM was flush against the face of the machined scintillator paddle. Further details regarding the three coupling intervals shown in Fig. 13 are discussed further in Ref. [1]. The results of this study are illustrated in Fig. 13.

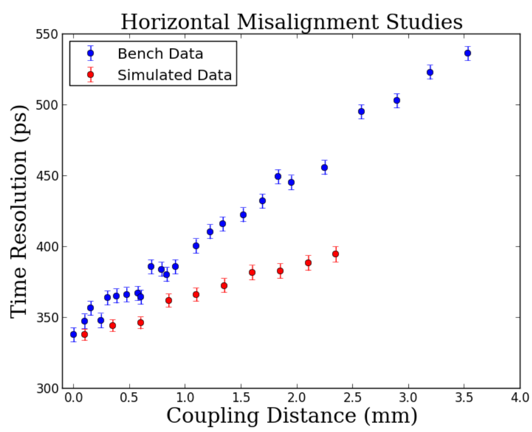

Figure 13: Coupling distance studies. It is useful to note that at a coupling distance of 251 μm the time resolution was identical to what was measured in Fig. 12 while conducting the vertical alignment studies.

The slight disagreement between bench data and simulation observed at large coupling distances ($>$ 1mm) in the horizontal misalignment studies is attributed to a systematic error in which the active area of the SiPM was not parallel to the upstream end of the scintillator paddle during these measurements. It is clear from the data that the optimal coupling range was 50 μm $<$ z $<$ 350 μm and there was no significant reduction in time resolution performance or light collection over a 0 μm $<$ z $<$ 600 μm range.

5. Fabrication

In order to successfully identify the 2 ns electron beam bunch structure delivered by the CEBAF to within 99% accuracy, the GlueX Start Counter time resolution is required to be $<$ 350 ps. In the following section the details of polishing and characterizing machined scintillators, as well as the construction of the Start Counter are discussed.

5.1. *Polishing Machined Scintillators*

The surfaces of the machined scintillators incurred a plethora of surface defects and chemical contaminants known to harm scintillator surfaces while undergoing edge polishing at McNeil Enterprises. Therefore, in an effort to recover the performance capabilities, polishing was required.

To polish the machined scintillator surfaces, Buehler Micropolish II deagglomerated 0.3 μm alumina suspension was utilized [14]. The polishing suspension was diluted with a 5:1 ratio of de-ionized H_2O to alumina and applied to a cold, wet $6'' \times 0.5''$ Caswell Canton flannel buffing wheel [15] operated at < 1500 RPMs. All surfaces of the scintillators were carefully buffed until all large, uniform surface defects were removed. In order to eliminate small localized surface defects, hand polishing with a soft NOVUS premium Polish Mate microfilament cloth [16] and diluted polishing suspension was applied. These polishing procedures made the scintillators void of virtually all scratches and surface defects. Further details of the aforementioned polishing procedures are discussed in [1].

Once the appropriate polishing procedures had been developed and implemented the surface quality was greatly improved as can be seen in Fig. 14 which illustrates the same scintillator paddle before and after polishing. A red laser beam was shone

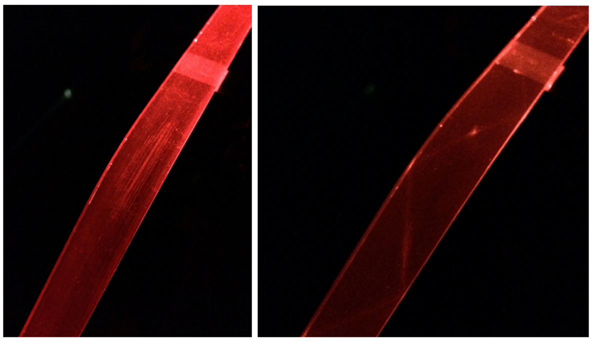

Figure 14: Effects of polishing scintillators. Left: non-diffuse laser incident on an edge, before polishing, at the upstream end of the straight section. Right: non-diffuse laser incident on the same edge, after polishing, at the upstream end of the straight section.

into the scintillator medium from the upstream end aimed at one edge so that the total internal reflection towards the tip of the nose was visible. The unpolished scintillator had such poor surface quality that the reflections in the bend region could not be seen due to the multiple scattering of light at the scintillator boundaries. However, the reflections in the polished scintillator can clearly be seen traversing down through the nose region. On average, at the tip of the nose, the scintillators exhibited a $\approx 15\%$ improvement in time resolution. Moreover, a substantial reduction of erratic fluctuations in performance of the scintillators was observed.

5.2. *Testing*

The polished scintillators were tested in order to determine their light output and time resolution properties. They were measured in an identical and reproducible manner utilizing a custom fabricated test stand shown in Fig. 15. The test stand fa-

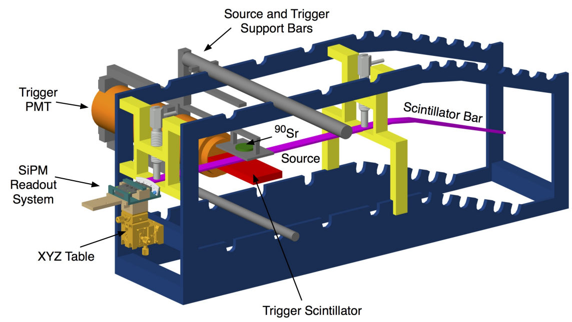

Figure 15: CAD Drawing of the scintillator test stand.

cilitated the precise measurement of the aforementioned scintillator properties at 12 well-defined locations (blue) along the length of the scintillator paddles. Specifically four locations in the straight section, three in the bend, and five in the nose were tested.

The measurements were conducted with a collimated ^{90}Sr source oriented orthogonal to the wide flat surface of the scintillators. The ^{90}Sr source provided minimum ionizing electrons ranging in energy from $0.5 - 2.3$ MeV *via* beta-decay [17][18]. A trigger photo-multiplier tube was placed underneath the scintillator on the opposite side of the ^{90}Sr source and provided the TDC start time and ADC gate. A SiPM detector array identical to the ones installed in the final ST assembly, was used for readout.

The signals from the SiPM and the trigger PMT were then recorded in our data acquisition computer configured with the CEBAF on-line data acquisition (CODA) software. 10,000 event triggers and associated data were collected at each of the locations along the scintillator path. Subsequently, the ADC and TDC data were analyzed to measure the light output and time resolutions respectively of the whole lot of polished machined scintillators.

Once the 30 machined scintillator paddles which exhibited the best time resolution and light output properties from the lot of 50 were selected, they were carefully wrapped in Reynolds food grade aluminum foil. The aluminum foil is 16.5 μm thick and possesses good reflectivity properties. Moreover, the aluminum foil protects the surfaces of the scintillators during both the testing and assembly processes.

The measured time resolutions for the 30 best scintillators, which comprise the ST, were found to be satisfactory and even well below design resolution in the nose region which is illustrated in Fig. 16.

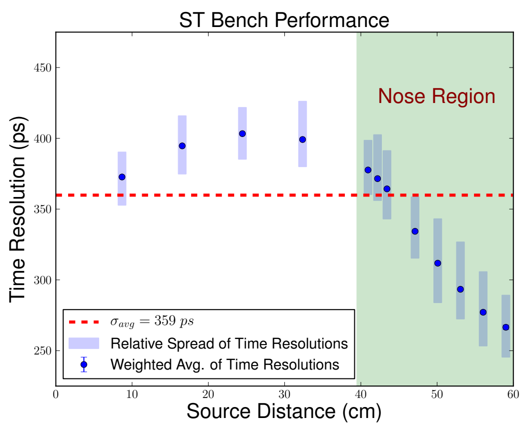

Figure 16: Weighted average of the time resolution of 30 the best scintillator paddles versus the source distance from the SiPM as measured on the bench. The shaded vertical blue boxes indicate the relative spread of the time resolutions among each of the 30 paddles. The dashed line indicates the weighted average of all 30 paddles for the 12 data points collected for each paddle. The horizontal dashed red line indicates the total weighted average across the full length of the 30 paddles. These data correspond to the paddles which were utilized in the fabrication of the Start Counter.

The unique geometry of the machined scintillator paddles exhibit the aforementioned phenomenon of an increase in light collection in the nose region as the light source moves towards the tip at the downstream end. It is hypothesized that the relatively poor time resolution in the straight section is due to a reflective smearing effect in which light is able to traverse from the straight section down to the tip of the nose, and then back up to the upstream end.

5.3. Assembly

In order to assemble the ST an assembly jig, illustrated in Fig 17, was fabricated. The jig consisted of a rotating cylindrical mounting bracket rigidly attached to a 2" diameter shaft housed in two cast iron mounted steel ball bearings. The rotating bracket was engineered such that it was free to rotate unless engaged by a spring loaded locking plunger which caused the assembly jig to move in discretized 12° intervals. This provided the ability to orient scintillator paddles parallel to the table top so that alignment and coupling could be performed in a reliable and reproducible manner.

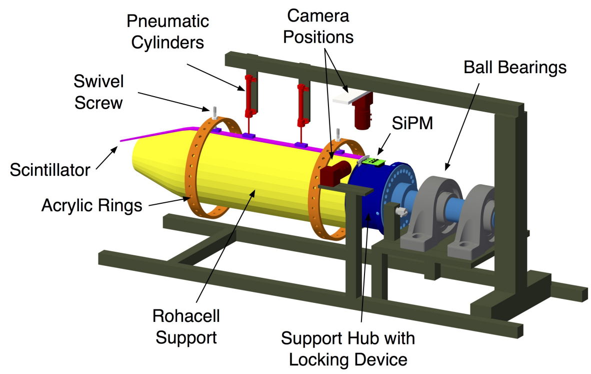

Figure 17: CAD drawing of the ST assembly jig.

While mounted to the assembly jig, the upstream chassis and Rohacell was attached to the rotating bracket. A vertical bar running parallel to the table above the Rohacell served as a mount for the pneumatic cylinders so that the scintillators could be held firmly in place during installation. Furthermore, it provided a surface in which a portable flex arm could hold a machine vision camera to monitor the coupling of the scintillators and SiPMs.

A pressurized gas system was implemented to provide manual control of the two pneumatic cylinders with soft, semi-dense rubber feet attached to the ends. The rubber feet would hold the scintillator being installed firmly in place by activating two switches which controlled each pneumatic cylinder independently *via* bi-directional solenoids connected in a 5 psi nitrogen gas system.

Two free floating acrylic rings, with 30 tapped holes 12° apart, were fabricated so as to firmly hold the scintillator paddles in place during assembly. Each tapped hole housed a 10° swivel pad thumb screw which had silicone foam foot (0.25×0.25 in^2) adhered to it in order to provide a soft barrier between swivel pad and the scintillator surface.

The camera, seen in Fig. 18, and its associated software were utilized to both measure and control the scintillator/SiPM coupling distances as well as the shimming heights with a precision of < 10 μm in real time. The camera was calibrated such that

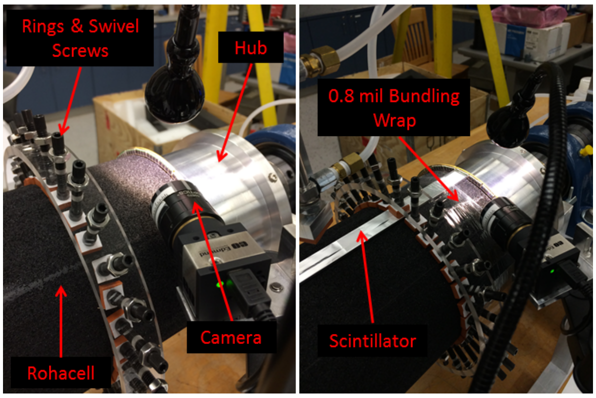

Figure 18: Aligning ST1 to support hub. Left: CMOS camera and lamp prepared to monitor ST1 positioning. Right: Reference scintillator wrapped to Rohacell during ST1 alignment.

at various magnification settings the distance to pixel ratio was known. The 10 ST1 boards were mounted to the pre-fixed tapped holes along the lip of the upstream support hub. Black 1 mm spacers were installed between the ST1 PCB and the support hub to avoid any possibility of the electrical contact between the two. The position of the ST1 was adjusted such that the distance between the top edge of the scintillator and the top edge of the active area of the SiPM was offset by 30 mils (762 μm).

On average each paddle required 30 mils of Kapton polyimide heavy duty film (type HN, $\rho = 1.42$ g/cm^3) radial shimming. Moreover, the scintillators were coupled to the SiPM's at a distance of $<$ 200 μm. More details regarding the assembly process are discussed in Ref. [1].

In order to make the ST light tight, an inner cone of black Tedlar polyvinyl fluoride $\rho \approx 1.5$ g/cm^3 [19] was taped to the Rohacell as seen in Fig. 19. A few gaps existed in the Rohacell at the glue joints, and were filled in with black RTV silicone caulking. Moreover, it was painted with black latex

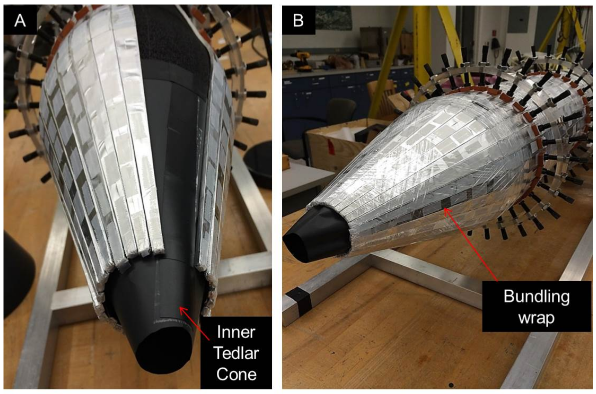

Figure 19: Inner Tedlar cone. Shown is before (a) and after wrapping with bundling wrap (b). The cone was specifically engineered to have the same dimensions of the Rohacell support structure to avoid crumpling of the light tightening material.

paint for light tightening purposes. The support hub was also was wrapped with Tedlar and taped down with black electrical tape. The spacing between the ST1 PCBs along with the bottom side of the support hub, was filled with RTV black opaque silicone caulking. Similarly, RTV silicone caulking was then applied to the inner edge of the collar which encompassed the ST1 PCBs at their outer diameter.

In order to secure paddles to the Rohacell support structure the Start Counter was wrapped along its length using self-adhesive transparent bundling wrap (0.8 mil thick, 6 in wide) at six different locations perpendicular to the central axis of rotation. Four locations were wrapped along the straight section at equal distance (≈ 8 cm) from one another, one in the bend and one in the nose section. Five layers of bundling wrap were applied to each section.

A cone of Tedlar was wrapped around the nose region and taped down with electrical tape as seen in Fig. 20. The tips of the inner and outer cones in the nose region were then taped together with electrical tape and trimmed of excess material. Furthermore, a cylindrical piece of Tedlar was taped down at the bend region and to the collar covering the ST1 boards. The fully assembled and cabled ST mounted to the GlueX liquid H_2 target can be seen in Fig. 20.

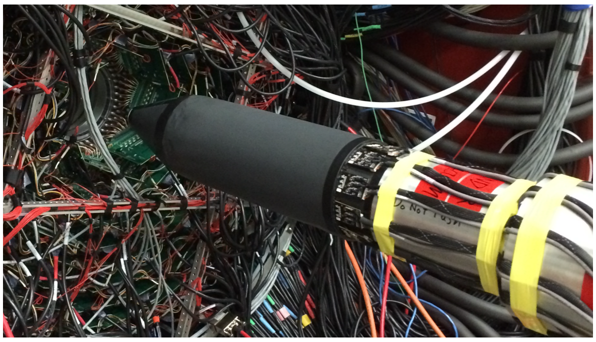

Figure 20: Light tight Start Counter mounted to the GlueX liquid H_2 target. The beam direction is from right to left and travels down the sentral axis of the ST. During operation the ST resides in the bore of the superconducting solenoid magnet which is visible in the top left corner.

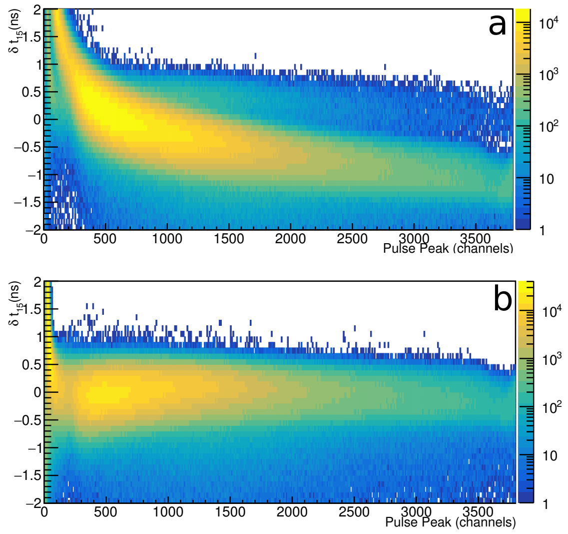

Figure 21: a) Single paddle time-walk spectrum, b) post walk correction. Plotted on the vertical axis is δt and on the horizontal axis is the corresponding pedestal subtracted pulse amplitude spectrum. The red line shown in a) is a least squares fit to the time-walk spectrum.

6. Calibration

In this section the various calibration procedures taken in order to minimize the time resolution and enhance both the particle identification (PID) and time of flight (TOF) capabilities of the Start Counter are discussed.

6.1. Time-walk Correction

The time-walk effect is a well understood consequence of leading edge discriminators (LED). Analog signals of varying amplitudes crossing a fixed threshold, as determined by the discriminator threshold setting, will do so at varying times. Thus, the corresponding logic signal output from the LED will "*walk about*" in time, resulting in an undesirable smearing of the measured ST TDC times.

The FADC250's provide a high resolution pulse time (62.5 ps/channel) that is time-walk independent [1] [20]. Therefore, for events in which both the FADC and TDC register hits in the same channel, the pulse time can serve as a reference time for that event. The TDC/FADC time difference is given by Eq. 1 where i is the paddle number index.

$$\delta t_i = t_i^{TDC} - t_i^{FADC} \tag{1}$$

The FADC250's return both the amplitude and integral of events which are above the programmed threshold [20]. Since the amplitude better characterizes the rise time of the ADC pulse profile as compared to the pulse integral, it was selected for the time-walk corrections. Figure 21 (a) shows a typical time-walk spectrum, *i.e.* δt versus the pulse amplitude, for one sector of the ST. This correlation is nonlinear and requires a polynomial functional form to describe it which is given by Eq. 2 from Ref. [21].

$$f_i^w\left(a/a_i^{thresh}\right) = c0_i + \frac{c1_i}{(a/a_i^{thresh})^{c2_i}} \tag{2}$$

In Eq. 2 f_i^w is the functional form of time-walk fit for the i^{th} sector, while a and a_i^{thresh} are the pulse amplitude and discriminator threshold converted to ADC units respectively. Furthermore, $c0_i, c1_i, c2_i$ are the time-walk correction fit parameters. This empirical function was chosen so that as the pulse amplitude increases, the correction function will asymptotically approach a constant, namely $c0_i$. Therefore, at large pulse amplitudes the correction f_i^w for δt_i will reduce to an effective offset. Moreover, signals with small amplitudes will have δt_i, corrected *via.* f_i^w, so as to match the signals with large amplitudes. Thus, signals of varying amplitude will exhibit a constant δt_i as desired.

The data in Fig. 21 (a) were fit using Eq. 2 and ROOT's MINUIT χ^2 minimization fitting library [22] for pulse peak values ranging from [50, 2100]. An identical fit was carried out for each of the ST sectors.

The most probable value (MPV) of the minimum ionizing peak, as observed *via.* the pulse amplitude spectra, was chosen to be the location in which the time-walk correction is zero. This location effectively serves as a reference point for the correction. The MPV (a_i^0) was determined on a sector by sector basis by simply acquiring the pulse peak channel bin which had the most number of entries after the pulse peak channel 200. The large spike in the pulse peak spectrum at very low pulse peak values are due to various electromagnetic background events clipping threshold and do not correspond to a true minimum ionizing particle traversing the scintillator medium.

Once the necessary time-walk correction parameters are determined, the correction is applied to the TDC time and is given by Eq. 3.

$$T_i^w = t_i^{TDC} - f_i^w(a/a_i^{thresh}) + f_i^w(a_i^0/a_i^{thresh}) \quad (3)$$

With the time walk corrections having been applied, the corrected timing distributions appear much more uniform in nature and exhibit a factor 1.75 improvement in resolution [1]. Fig. 21 (b) illustrates the vast improvement in the time difference spectrum (δt) as a result of the applied time-walk corrections.

6.2. Propagation Time Corrections

As a charged particle traverses through the ST scintillator material the molecules become excited and a small fraction ($\approx 3\%$) [23] of the excitation energy is released in the form of "optical" photons. The photons produced will be emitted uniformly in all directions and some will escape the medium, some will be reflected back into the medium by virtue of the reflective Al foil wrapping, and some will be lost for detection. However, the majority of detected photons will have undergone many total internal reflections while they propagated from their source to the SiPM detector placed at the upstream end. The time between production in the ST scintillator paddles and detection is position dependent and must be accounted for and is discussed below.

The EJ-200 scintillator material has a refractive index of 1.58 [3] and the corresponding speed of light is $\approx$ 19 cm/ns. However, what is measured in the lab is known as the effective velocity which is slower due to the fact that the majority of photons are not traveling in straight lines parallel to the medium boundaries. Instead they are constantly reflecting off the boundaries resulting in increased respective path lengths which contributes to a reduced velocity known as the effective velocity.

Correcting for the time in which light spends traversing through the scintillator material is a necessary correction since the ST paddles are 60 cm in length. Thus, light produced in the tip of the nose will take on the order of 4 ns to reach the SiPM at the upstream end. Performing the propagation time corrections utilizing the common effective velocity method is not the most robust procedure for the case of the ST. Studies performed with simulation and data showed that the unique geometry in the nose causes the effective velocity of light to be larger than that of the straight section and therefore they must be treated in an independent manner.

In order to conduct the propagation time corrections for the ST a distinct set of events needed to be selected so that a well defined reference time was being utilized. This reference time was utilized as a measure of the event time for all other charged tracks intersecting the ST within the same event.

For every charged track in a given event, two global tracking requirements were required. First, only charged tracks with a good tracking confidence level were considered. Secondly all charged tracks were required to have their vertex located within the target and radially within 1 cm from the beam. Only tracks passing these conditions were considered for analysis.

At least two specific tracks were required in each event in order to conduct the ST propagation time corrections. One track that has hit the time of flight (TOF) detector and not the ST provides the reference time for that event. All subsequent tracks were required to intersect the ST and not the TOF and were used to provide the ST measure of the vertex time for that event. This was done in order to avoid any potential bias in the calibration.

The advantage of using the time associated with a track matched to the TOF is that the time resolution of the TOF is the best of any detector in Hall-D ($\approx$ 96 ps) [24]. The calibrated (time-walk & propagation) hit time returned by the TOF (T_{hit}^{TOF}) was then corrected for the flight time from the track vertex to the TOF (T_{flight}^{TOF}). Equation 4 is the TOF measure of the track vertex time.

$$T_{vertex}^{TOF} = T_{hit}^{TOF} - T_{flight}^{TOF} \quad (4)$$

In order to determine the time in which the beam bunch arrived at the interaction point (T_{vertex}^{BB}) the T_{vertex}^{TOF} time must first be corrected for the RF measure of the vertex time (T_{vertex}^{RF}). The steps required to correctly calculate T^{BB}_{vertex} are discussed in detail in Ref. [1]. For every event, the first track satisfying the aforementioned fiducial track selection and is matched to the TOF will then have the associated T^{BB}_{vertex} time calculated. This time serves as the reference time for all other tracks that have intersected the ST in that event.

In order to properly calculate the propagation time (T^{ST}_{prop}) of photons produced by a charged track intersecting the ST, a few quantities must be known. Particularly the time-walk corrected hit time (T^{ST}_{hit}), the flight time from the track vertex to the ST intersection point (T^{ST}_{flight}), and a well defined reference time corresponding to the event (T^{BB}_{vertex}). With the reference time determined, all other charged tracks passing the previously discussed fiducial track selection and which have a match to the ST (and not the TOF) are analyzed. Equation 5 illustrates the ST measure of the vertex time.

$$T^{ST}_{prop} = T^{ST}_{hit} - T^{ST}_{flight} - T^{BB}_{vertex} \tag{5}$$

This time difference is a direct measure of the amount of time the detected light produced by the intersecting charged track spent traversing the scintillator medium. In order to perform the propagation time corrections the z-coordinate of the tracks intersection point with the ST (z^{ST}_{hit}) was also recorded for every charged track intersecting the ST relative to the upstream end. However, z^{ST}_{hit} only provides information of where the track intersected the ST along the z-axis and is not an accurate measure of the distance from the SiPM readout to the source of the scintillation light due to the unique ST paddle geometry. This distance, d^{ST}_{hit}, was calculated for each for each z^{ST}_{hit} directly while taking into account the paddle geometry.

Once both T^{ST}_{prop} and d^{ST}_{hit} were calculated, the propagation correction calculation could be performed. Figure 22 (a) illustrates the correlation between these two quantities. The calculated propagation times were then grouped into three distinct regions corresponding to the three unique geometrical sections of the ST namely the straight, bend, and nose regions. The correlations seen in Figure 22 (a) for these three regions were then fit utilizing the χ^2 minimization technique with a linear function whose functional form is given by Eq. 6 where the index j indicates which region the fit is being performed relative to the i^{th} paddle.

$$f^i_j(z) = A^i_j + B^i_j \cdot z \tag{6}$$

With the fit parameters determined, an explicit time difference correction for each of the ST sectors could then be applied to calculate the ST measure of the vertex time given by Eq. 7.

$$T^{ST}_{vertex}(z) = T^{ST}_{hit} - T^{ST}_{flight} - T^{ST}_{prop}(z) \tag{7}$$

Figure 22 (b) illustrates the propagation time corrected time as a function of the distance between the SiPM readout and the source of the scintillation light along the path of the ST paddles. With the propagation time corrections applied it is clear that the ST time is no longer dependent on the where the charged track intersects with the paddles as expected. The ST corrected time now provides an accurate measure of the vertex time for the track in the event and is discussed further in Sec. 7.

6.3. Attenuation Corrections

The measured energy deposited (dE_{meas}) from a charged particle traversing a scintillator medium is proportional to the number of photons created, which is in turn proportional to the integrated pulse read out by the FADC250. However, since the photons created *via.* ionization can be lost through scattering, absorption, or escape at the boundaries as they propagate through the scintillator medium, the energy deposition measured by the SiPM does not correctly measure the energy deposited by the charged particle at the location of intersection with the scintillator and therefore must be corrected.

One can define an *attenuation coefficient* which characterizes a particular materials ability to absorb photons. The attenuation coefficient is defined to be the length in the medium in which the initial number of primary photons are reduced by a factor of $1/e$ (36.8%). Since the loss of photons in scintillators equates to the loss of information relative to the event of interest, it is desirable to have a scintillator material with a long attenuation length. For reference a flat $2 \times 20 \times 300$ cm^3 EJ-200 scintillator has a relatively long attenuation length on the order of 4 m [3].

In order to determine the attenuation coefficients of interest, tracks hitting the ST which passed identical fiducial track selection cuts as discussed in Sec. 6.2, were selected for analysis. Furthermore, the tracks pedestal subtracted pulse integral (PI), track length inside the scintillator medium (dx), energy deposition (dE_{meas}), track momentum (p), and the z-component of the tracks intersection point with the ST relative to the upstream end (z^{ST}_{hit}), where the SiPM is located, were recorded.

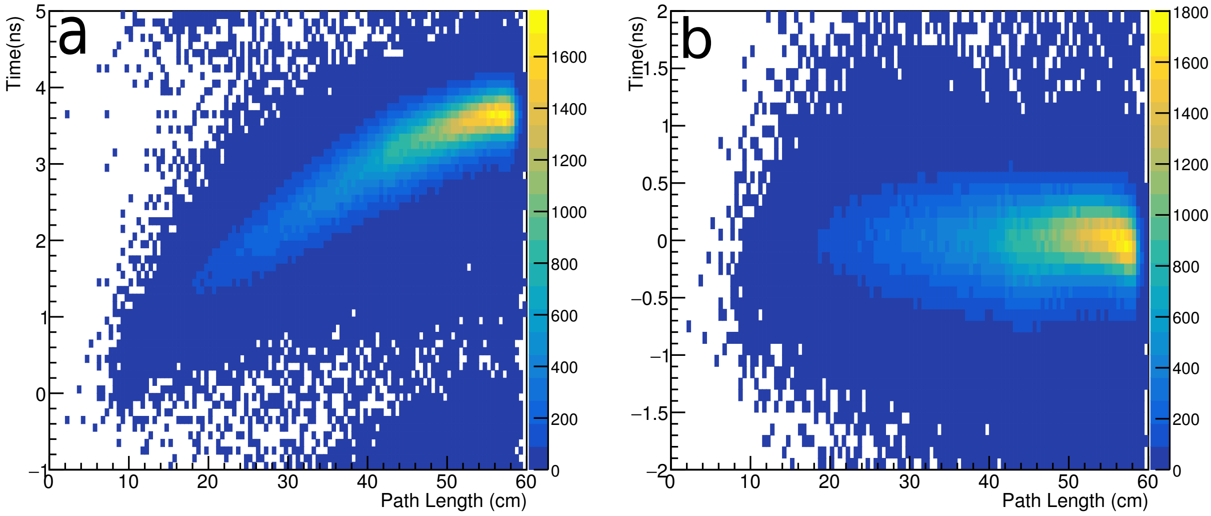

Figure 22: a) Single paddle propagation time correlation. T^{ST}_{prop} is plotted on the vertical axis and d^{ST}_{hit} is plotted along the horizontal axis. There is a clear correlation between the time in which optical photons are detected by the SiPM and the location of the scintillation light along the length of the paddle. b) Single paddle propagation time after correction.

A plot of the uncorrected energy deposition per unit length versus the track momentum for tracks matched to the ST are shown in Fig. 23. It is clear

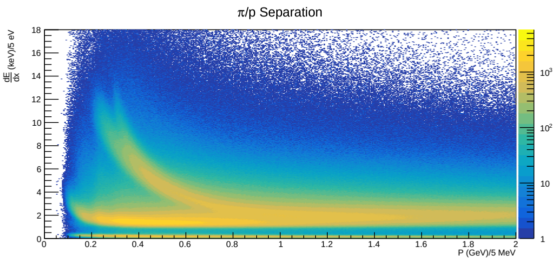

Figure 23: Typical uncorrected dE/dx $vs.$ p distribution in the Start Counter. The "banana band" corresponds to protons while the horizontal band corresponds to charged electrons, pions, and kaons.

that no reliable PID can occur for tracks with $p > 0.6\ GeV/c$.

The pedestal corrected pulse integral (PI) data, normalized to the path length dx of the track in the scintillator medium, were binned in 3.5 cm z^{ST}_{hit} bins along the full length of the paddle. In order to properly quantify the amount of scintillation light created in the event, the most probable value (MPV) of the PI was extracted utilizing an empirical function which is both continuous and differentiable is given by equation 8.

$$f(z) = p_0 e^{(-p_1(z-p2))} \times (1 + \tanh(p_1(z - p2))) \quad (8)$$

A fit to the data in a single 3.5 cm z^{ST}_{hit} bin is illustrated in Fig. 24. Once the fits were successfully

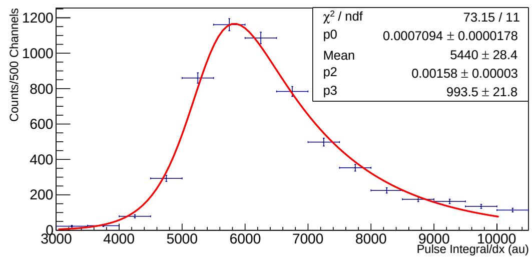

Figure 24: Pedestal subtracted pulse integral integral data normalized to the the track length in the scintillator medium for a single 3.5 cm bin along the paddle length.

performed the MPV was extracted analytically and then plotted against the average value for each z^{ST}_{hit} bin as seen in Fig. 25. With the above data in hand, one can quantitatively measure the attenuation of photons in the ST scintillators and is discussed below.

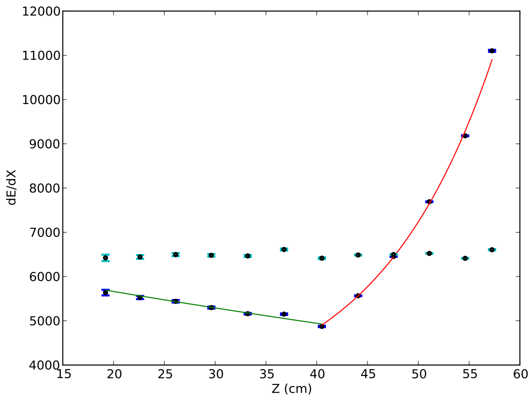

Figure 25: Fits to the attenuation data.

As was discussed in Sec. 3.2 the unique geometry of the ST is comprised of two distinct regions, *i.e* the straight and nose sections. These sections have differing properties in terms of light output and thus, time resolution. Therefore, when performing attenuation corrections the two regions were treated independently in order to properly characterize photon attenuation. It was empirically determined that the ideal fit function was piecewise discontinuous and follows Eq. 9.

$$f_d^i(z) = \begin{cases} A_S^i e^{-B_S^i \cdot z} & z < 39.5cm \\ A_N^i e^{B_N^i \cdot z} + C_N^i & z > 39.5cm \end{cases} \quad (9)$$

Exponential decay functions are typically used to describe the attenuations of photons in scintillator material. However, for the unique case of the nose section, an exponential growth function was utilized. It is clear from Fig. 25 that the aforementioned exponential functions, corresponding to their respective geometrical sections, fit the data in a robust manner.

Since a piecewise discontinuous function was required to describe the attenuation data, the intersection of the two exponential fit functions was calculated (Z_b^i) so that the corrections applied were piecewise continuous and is given by Eq. 10.

$$f_c^i(z) = \begin{cases} A_S^i e^{-B_S^i \cdot z} & z < Z_b^i \\ A_N^i e^{B_N^i \cdot z} + C_N^i & z > Z_b^i \\ A_S^i e^{-B_S^i \cdot Z_b^i} & z = Z_b^i \\ A_N^i e^{B_N^i \cdot Z_b^i} + C_N^i & z = Z_b^i \end{cases} \quad (10)$$

Evaluating the fit function in the straight section at $z = 0$ cm is representative of a minimum ionizing particle traversing through the upstream end closest to the SiPM readout. In this instance the detected photons traverse through virtually no scintillator material, and are thus subject to no effects of attenuation. Therefore, for all charged particles passing trough the ST scintillator paddles we apply an attenuation correction factor ($R^i(z)$) to the deposited energy measurement (dE_{meas}) to preserve the information regardless of where the track intersects the paddles.

The corrected energy deposition ($dE^i_{corr}(z)$) for paddle i is given by Eq. 11.

$$dE^i_{corr}(z) = dE_{meas} \cdot R^i(z) = dE_{meas} \cdot \frac{f_c^{15}(0)}{f_c^i(z)} \quad (11)$$

It is required to note that paddle 15 was chosen as a reference paddle in an arbitrary manner. Thus, for all tracks intersecting the full length of the ST we obtain the following relationship, seen in Eq. 12, as desired.

$$f_c^i(z) \cdot R^i(z) = A_S^{15} \; \forall \; z \in \; [0, 60] \; (cm) \quad (12)$$

Once all energy deposition measurements have had the appropriate attenuation corrections applied as was discussed above, the PID capabilities of the ST are considerably enhanced and are discussed further in Sec. 7.

7. Performance

The Start Counter was installed in Hall-D just prior to the Fall 2014 GlueX commissioning run. It was not until the Spring 2015 commissioning run that enough statistics were obtained with an LH_2 target to perform reliable calibrations. With the aforementioned data set, the procedures to calibrate the detector and measure it's performance were developed and deployed.

As was discussed in previous sections, the geometry of the ST nose section results in an increase of the light output as the scintillation source moves towards the downstream end. While investigating FADC250 data under nominal beam conditions, this phenomenon was immediately observed through the pulse amplitude and pulse integral data. Figure 26 illustrates that similar to the bench measurements the light output increases exponentially as the scintillation source moves towards the downstream end. This feature of the ST geometry is quite advantageous since the majority of the

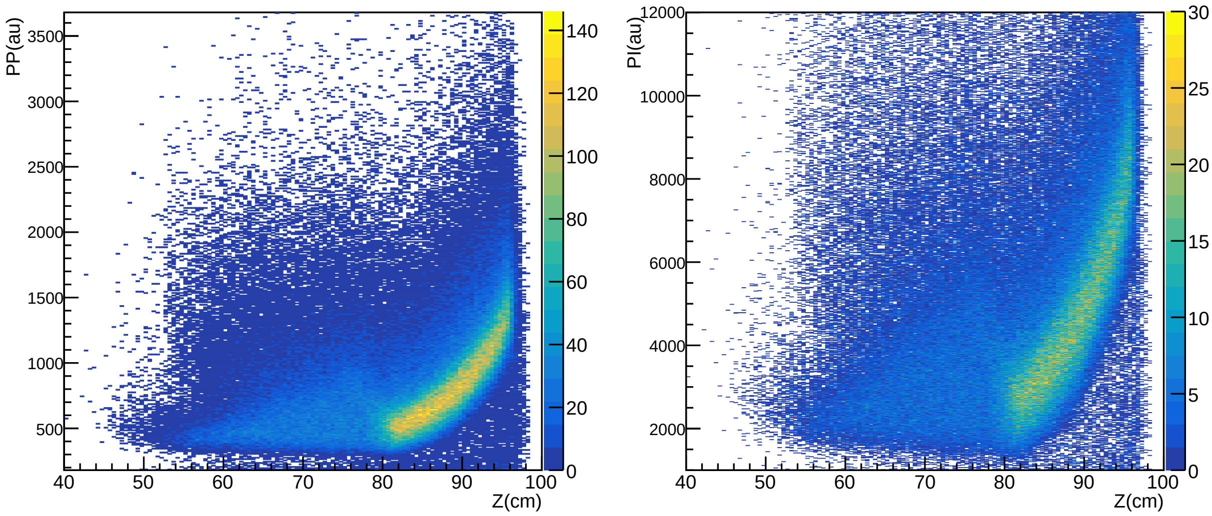

Figure 26: FADC spectra from the Spring 2017 run. Left: pulse amplitude versus the z-intersection of charged tracks matched to the ST. Right: pulse integral versus the z-intersection of charged tracks matched to the ST. The straight section corresponds to 40 cm $< z <$ 80 cm, the bend section 80 cm $< z <$ 84 cm, and the nose section 84 cm $< z <$ 98 cm.

charged tracks produced under the nominal GlueX beam conditions intersect the ST in the nose region and therefore have the largest light amount of light collected by the SiPM's as the upstream end.

Once the proper attenuation corrections were applied to the data, the PID capabilities of the ST were greatly enhanced. Figure 23-b illustrates the PID capability of charged tracks intersecting the ST. As compared to Fig. 23-a, the reliable separation of protons and other hadrons occurs for charged tracks with $p < 1.1\ GeV/c$ which is a factor two improvement from the uncalibrated data.

After the previously discussed time-walk and propagation time corrections were complete, it was then possible to utilize the ST to measure the time of charged track vertices for tracks that are matched to the ST. The vertex time is defined to be the time in which a polarized Bremsstrahlung photon interacted with the LH_2 target and produced a charged track that intersected the ST. An identical charged track selection process as outlined in Sec. 6.2 was utilized so that the time resolution of tracks matched to the ST could be measured.

The equation to calculate the ST measure of the vertex time is given by Eq. 5. The resulting distribution in the time difference of these times provides a measure of the ST time resolution and is seen in

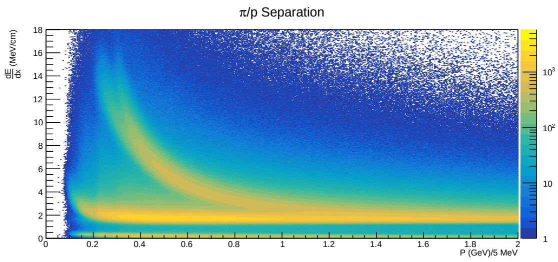

Figure 27: Typical corrected dE/dx $vs.$ p distribution in the Start Counter. Shown is the corrected dE/dx $vs.$ p distribution for tracks matched to the Start Counter in the Spring 2017 run. The "banana band" corresponds to protons while the horizontal band corresponds to charged electrons, pions, and kaons. It is clear that pion/proton separation is achievable for tracks with $p < 1.1\ GeV/c$.

Fig. 28.

The aforementioned fits were then carried out for each of the ST sectors with σ, and its associated error being calculated. Then a weighted average of the 30 σ's were calculated so that the ST could have its time resolution characterized in its entirety. The same procedure was also conducted for the three individual sections. Figure 29 illustrates the uniformity in time resolution among all sectors of the ST. It indicates also that the average time resolution of

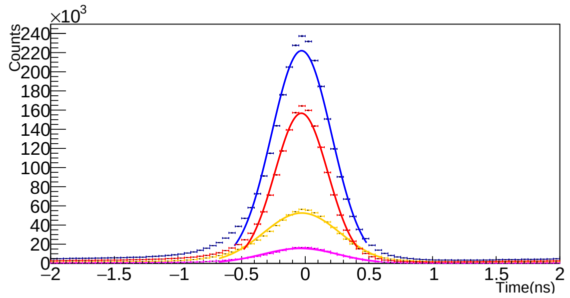

Figure 28: Typical Start Counter/RF time resolution distribution. Shown is the time resolution distribution for sector 15 during the Spring 2017 run 30279. The x-axis is the time difference between T^{ST}_{vertex} and T^{BB}_{vertex}. The orange histogram is the resolution in the straight section. The magenta and red histograms correspond to the resolution in the bend and nose sections respectively. The blue histogram is a sum of the three sections and corresponds to the resolution along the entire length of the paddle.

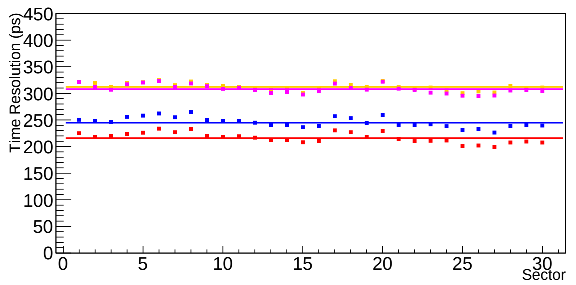

Figure 29: ST time resolutions as a function of sector number (Blue line). Orange and magenta lines are the average time resolution for the straight and bend sections respectively. The nose section resolution is greatly enhanced due to the exponential increase in light output (red).

245 ps is well below the design resolution of 350 ps.

Table 1 details the weighted average time resolution of all the ST sectors in the different geometrical regions.

It is clear from Table 1 that what is observed is that measurements made with beam data exhibit the same phenomenon of substantial improvement in light collection, and thus time resolution, as light is produced further downstream in the nose region.

When these time resolution measurements were conducted with data collected in Spring 2017, approximately 3 years had elapsed since the paddles were first tested on the bench at FIU. Prior experience with degrading scintillators indicates that

Section	$\sigma_{\mathbf{all}}$	$\sigma_{\mathbf{straight}}$	$\sigma_{\mathbf{bend}}$	$\sigma_{\mathbf{nose}}$
$\sigma_{\mathbf{avg}}$	245 ps	314 ps	309 ps	216 ps

Table 1: Average time resolutions by section. Shown is the average of all 30 ST sectors by independent geometrical regions.

degradation in time resolution will be visible in a matter of weeks. However, after 3 years no degradation has been observed and the ST is still performing well below design resolution.

8. Conclusion

The GlueX Start Counter was designed and constructed at Florida International University for use in Hall-D at TJNAF to provide separation of the 500 MHz photon beam bunch structure delivered by the CEBAF to within 99% accuracy. It is the first "start counter" detector to have utilized magnetic field insensitive SiPMs as the readout system. Despite the many design and manufacturing complications, the ST has proven to have performed well beyond the design timing resolution of 350 ps with an average measured resolution of 280 ps. Furthermore, the capabilities of the ST make it a viable candidate to assist in PID calculations.

The unique geometry of the ST nose section has illustrated the advantage of tapering trapezoidal geometry in thin scintillators. Through simulation, tests on the bench, and analysis of data obtained with beam it has been definitively demonstrated that this geometry results in a phenomenon in which the amount of light detected increases as the scintillation source moves further downstream from the readout detector.

Since it's installation in Hall-D during the Fall 2014 commissioning run, the ST has shown no measurable signs of deterioration in performance. This suggests that the ST scintillators are void of crazing and will most likely be able to meet and exceed the design performance well beyond the scheduled run periods associated with the GlueX experiment.

It is planned to incorporate the ST into the level 1 trigger of the GlueX experiment for high luminosity ($> 0.5\ \mu A$) running. Preliminary studies suggest that the high efficiency ($> 95\%$) of the ST, in combination with the calorimeters, provides good suppression of electromagnetic background in regards to the level 1 trigger. Furthermore, the ST's high degree of segmentation has shown to suppress various background contributions associated with complex topologies while simultaneously providing precision timing information for reconstructed charged particles in GlueX.

9. Acknowledgments

The authors would like to graciously thank the plethora of Jefferson Lab staff members in both the Engineering division and Hall-D. Their numerous and invaluable contributions allowed for the Start Counter project to come to fruition. The authors would also like to extend their gratitude to the entire GlueX Collaboration who provided fruitful ideas and advice throughout the many stages of the project. Work at Florida International University was supported in part by the Department of Energy under contracts DEFG0299ER41065 and DE-SC0013620. Furthermore, this material is based upon work supported by the U.S. Department of Energy, Office of Science, Office of Nuclear Physics under Contract No.DE-AC05-06OR23177.

References

[1] E. Pooser, The GlueX start counter and beam asymmetry Σ in single π^0 photoproduction, Ph.D. thesis, Florida International University (2016).

[2] http://www.eljentechnology.com/.

[3] General Purpose Plastic Scintillator EJ-200, EJ-204, EJ-208, EJ-212, technical note available at http://www.eljentechnology.com/images/products/data_sheets/EJ-200_EJ-204_EJ-208_EJ-212.pdf.

[4] http://www.rohacell.com.

[5] http://www.mcnealplasticmachining.com/.

[6] http://www.hamamatsu.com/us/en/index.html.

[7] Multi-Pixel Photon Counter, technical note available at https://halldweb1.jlab.org/wiki/images/4/49/S10362-33_series_kapd1023e05.pdf.

[8] https://geant4.web.cern.ch/geant4/.

[9] K. S. Krane, Introductory Nuclear Physics, John Wiley & Sons, 1988, Ch. Detecting Nuclear Radiations, pp. 201–202.

[10] C. M. Poole, A cad interface for geant4, paper submitted to Cornell Archive (arXiv) May 5, 2011 (2011).
URL http://arxiv.org/pdf/1105.0963.pdf

[11] A. L. . C. Moison, A more physical approach to model the surface treatment of scintillation counters and its implementation into detect, paper presented at IEEE, Nuclear Science Symposium; Anaheim, November 2-4 available at http://geant4.slac.stanford.edu/UsersWorkshop/PDF/Peter/moisan.pdf (1996).

[12] https://www.newport.com/p/MT-XYZ.

[13] P. Khetarpal, Start counter: Optics simulations, talk Given at the February 16, 2012 GlueX Collaboration meeting (2012).
URL https://halldweb.jlab.org/DocDB/0019/001921/002/khetarpal_feb2012.pdf

[14] https://shop.buehler.com/consumables/grinding-polishing/polishing-suspensions/alumina-suspensions.

[15] http://www.caswellplating.com/buffing-polishing/buffing-wheels/canton-flannel-wheels.html#.

[16] https://www.novuspolish.com/polish_mates.html.

[17] ^{90}Sr Decay Radiation Data, national Nuclear Data Center, Nuclear Structure and Decay Database (NuDat) available at http://www.nndc.bnl.gov/nudat2/decaysearchdirect.jsp?nuc=90SR&unc=nds.

[18] ^{90}Y Decay Radiation Data, national Nuclear Data Center, Nuclear Structure and Decay Database (NuDat) available at http://www.nndc.bnl.gov/nudat2/decaysearchdirect.jsp?nuc=90Y&unc=nds.

[19] http://www.dupont.com/products-and-services/membranes-films/pvf-films.html.

[20] H. Dong, Description and Instructions for the Firmware of Processing FPGA of the ADC250 Boards Version 0x0C0D, fADC250 Manual Available at https://coda.jlab.org/drupal/system/files/pdfs/HardwareManual/fADC250/FADC250_Processing_FPGA_Firmware_ver_0x0C0D_Description_Instructions.pdf (February 2017).

[21] E. Smith, Low-level calibration constants for BCAL, technical note GlueX-doc-2618-v10, available at https://halldweb.jlab.org/DocDB/0026/002618/011/bcal_constants.pdf (December 2014).

[22] https://root.cern.ch/doc/master/classTMinuit.html.

[23] J. B. et al. (Particle Data Group), Review of particle physics, Phys. Rev. D 86 (010001) (2012) 342–343.

[24] B. Zihlmann, GlueX Time Of Flight Calibration, technical note GlueX-doc-2767-v4 available at `https://halldweb.jlab.org/DocDB/0027/002767/005/tofcalib.pdf` (July 2015).